Journal of Materials Chemistry A

ROYAL SOCIETY OF CHEMISTRY

PAPER

View Article Online
View Journal | View Issue

Cite this: J. Mater. Chem. A, 2025, 13, 34409

Synergistic and visualized toughening of elastomers through mechanophore crosslinks and multiple networks

Zeyu Wang, † Yongming Wang,† Ming-Chi Wang, Zehao Fan and Junpeng Wang *

Elastomers are essential in applications requiring high extensibility, yet their performance can be further enhanced through innovative design. A molecular design using multiple interpenetrating networks, where a brittle first network is isotropically prestretched by swelling in a stretchable matrix, dramatically increases toughness, primarily due to stress delocalization through bond scission in the sacrificial first network. In this work, we present a synergistic approach to elastomer design by employing anthracene–maleimide mechanophores as weak crosslinks in the first network of a multiple network elastomer. The interplay between mechanophores and multiple network structures not only improves the toughness but also enhances the mechanophore activity, achieving up to 37% activation in the triple network elastomer. The mechanofluorescence enables real-time visualization of bond scission, providing mechanistic insights into the toughening mechanism. Fluorescence imaging reveals significant mechanophore scission near the fracture surfaces of double and triple network elastomers. Mechanical and optical analyses indicate that the first network bears the majority of the load and that the mechanophore scission quantitatively correlates with the work of the fracture. This work demonstrates how mechanophores as weak crosslinks combined with multiple network topology synergistically enhance toughness and enable stress visualization, paving the way for damage-reporting, self-sensing elastomers with superior mechanical resilience.

Received 16th June 2025
Accepted 26th August 2025

DOI: 10.1039/d5ta04890g

rsc.li/materials-a

School of Polymer Science and Polymer Engineering, The University of Akron, Akron, Ohio 44325, USA. E-mail: jwang6@uakron.edu
† These authors contributed equally.

Junpeng Wang

Junpeng Wang received a B.S. in Chemistry from the University of Science and Technology of China (2010) and a PhD from Duke University under the guidance of Prof. Stephen Craig (2015). From 2016 to 2018, he worked as a postdoctoral fellow with Prof. Luping Yu at the University of Chicago and Prof. Jeremiah Johnson at the Massachusetts Institute of Technology. In 2019, he started his independent career at the University of Akron, where he is now an Associate Professor of Polymer Science. He has received a Sloan Research Fellowship and an NSF CAREER award. His research aims to address challenges in materials science by applying physical organic chemistry approaches.

Introduction

Elastomers are indispensable in a wide range of applications requiring high stretchability and durability, from automotive tires and industrial seals to soft robotics and wearable devices. However, traditional polymer networks often face a stiffness–toughness conflict, where crosslinks stiffen but embrittle them.[1–3] Innovative toughening strategies have been developed,[4–7] among which the multiple network (MN) strategy has emerged as a highly effective approach for reinforcing elastomers.[5,8] By incorporating a highly crosslinked, brittle first network that is prestretched within a loosely crosslinked, stretchable matrix network, MN elastomers achieve increased stiffness and toughness.[5,8] Toughening is accomplished by stress delocalization through bond scission in the sacrificial first network, thereby delaying the onset of crack propagation.[8,9]

Polymer mechanochemistry has emerged as a powerful field in materials science, offering innovative approaches for designing smart materials that respond to mechanical stimuli.[10–15] Recent advances have introduced the concept of mechanophores—molecular units that undergo specific chemical transformations when subjected to mechanical force—which have garnered significant attention.[16] While stress is typically considered destructive, mechanophores offer a unique

opportunity to turn stress into a productive outcome by enabling translation of mechanical energy into useful chemical responses. This capability provides unprecedented opportunities in self-healing materials,[17] damage reporting, stress sensing,[9,18–21] material mechanics[22–25] and controlled degradability.[26,27] However, the use of mechanophores in elucidating toughening mechanisms remains underexplored, with only a few pioneering studies, such as those by Creton and coworkers, addressing this gap.

The strategic placement of mechanophores within a polymer network can profoundly influence fracture toughness. Craig and co-workers demonstrated that in-chain mechanophores, which weaken network strands, can embrittle polymer networks.[28] In contrast, embedding non-scissile mechanophores within the strands enabled force-induced chain extension, leading to enhanced network toughness.[29] Similarly, strand lengthening through the dissociation of mechanophore crosslinks also resulted in significantly toughened elastomers.[30,31] This toughening mechanism, driven by force-triggered chemical reactions that lengthen polymer strands, highlights the critical role of mechanophore placement and reactivity in controlling mechanical properties.

Reinforcing elastomers without conventional inorganic nanofillers, such as silica or carbon black, ensures optical clarity, making it possible to detect and quantify bond scission *via* mechanoluminescence. Quantitative analysis of bond scission under mechanical loading is crucial for understanding the mechanics of polymer networks and guiding the design of tough, force-responsive materials. An ideal mechanophore for dual purposes of toughening and quantitative detection should be mechanically labile yet thermally stable, yielding a luminescent product upon activation that persists even after unloading. Anthracene–maleimide cycloadducts (AM) are stable up to 200 °C,[32] and undergo a mechanochemical retro-Diels–Alder reaction to liberate a fluorescent anthracene moiety.[19,33,34]

In this work, we developed a synergistic approach to elastomer design by integrating mechanophore crosslinkers with multiple network architecture. This strategy aimed to enhance toughness through preferential scission of mechanophore crosslinks in the first network, enable real-time visualization of bond scission *via* mechanofluorescence, and provide mechanistic insights into the toughening mechanism. Specifically, an AM mechanophore was employed as the crosslinker in the first network of an MN structure. Mechanical and optical analyses were conducted to investigate the correlation between mechanophore scission and toughness, while fluorescence imaging was used to map the spatial distribution of bond scission near the fracture surface. By combining mechanophores and multiple networks, this study sought to advance the understanding of toughening mechanisms and pave the way for the design of multifunctional elastomers with enhanced mechanical and optical properties.

Experimental

Materials

Ethyl acrylate (EA) was run through a plug of basic alumina (10 vol%) to remove the inhibitor and stored in a freezer for future use. Irgacure 819 and butanediol diacrylate (BD) were purchased from Sigma Aldrich and used directly. Chloroform was purchased from Fisher Scientific. Anthracene–maleimide Diels–Alder adduct diacrylate (AM) was synthesized according to the literature.[34]

Network synthesis

In a nitrogen-filled glovebox, AM (257.7 mg, 0.563 mmol, 1 equiv.) or BD (111.7 mg, 0.563 mmol, 1 equiv.) and Irgacure 819 (0.9 mg, 0.00225 mmol, 0.004 equiv.) were dissolved in degassed $CHCl_3$ (3 mL) and EA (6 mL, 56.3 mmol, 100 equiv.) in a scintillation vial. The solution was drawn into a syringe and injected into a customized mold. The mold was made of a silicone sheet (3788T21, McMaster-Carr) with a window cutout (140 mm × 135 mm × 0.5 mm), sandwiched between two well-cleaned glass plates (7″ × 7″ × 3/16″, 8476K17, McMaster-Carr). The four sides of the mold assembly were two-ply taped using 3M Super 88 inside and Temflex outside. Two needles (25G) were inserted into one side of the mold through the silicone, one for injection and the other for venting. After injection of the solution, both needles were taken out and the holes left by the needles were sealed with 3M Temflex. The mold was taken out of the glovebox and placed between two 365 nm UV lamps (wavelength = 365 nm, 100 W), separated by ~40 cm. Photopolymerization was allowed for 1 hour. The crosslinked network was carefully taken out of the disassembled mold and soaked in methanol at 40 °C for 10 minutes. It was then air-dried briefly and vacuum-dried at 70 °C for 4 hours to give the single network (SN).

SN was swollen in a monomer bath (100 mL) consisting of EA (100 equiv.), BD (0.01 equiv.) and Irgacure 819 (0.004 equiv.) in a wide-mouth glass jar, which was shielded from light in a cardboard box for 16 hours in a nitrogen-filled glovebox. The remaining solution was carefully decanted into a Ziploc bag and photopolymerized before disposal. The swollen gel was wiped off of excess liquid using Kimwipes and carefully placed between two glass plates (7″ × 7″ × 3/16″, 8476K17, McMaster-Carr), separated by a silicone sheet (inner dimensions: 160 mm × 160 mm × 1/32″, 3788T22, McMaster-Carr), secured with 3M Temflex tape and 8 sets of binder clips. The mold was taken out of the glovebox and placed between two UV lamps (wavelength = 365 nm, 100 W), separated by ~40 cm. The double network (DN) was formed by photopolymerization for 3 hours and was then dried *in vacuo* at 70 °C for 4 hours.

The triple network (TN) was synthesized following the same steps of DN synthesis except that two silicone sheets with different thicknesses (1/32″, 8602K51 and 0.5 mm, 3788T21, McMaster-Carr) were used together as the spacer.

The volume changes after each swelling–polymerization step were recorded and the prestretch ratio was calculated using the following equation:

$$\lambda_0 = (V_{MN}/V_{FN})^{1/3}$$

where V_{MN} and V_{FN} are the volume of the MN sample and the first network (FN), that is, the SN, respectively.

Fracture tests

Fracture tests were performed using the pure shear geometry on an Instron 5567. Each tested sample had a width of 20 mm and length of 15 mm, and the thickness varied from 0.73 to 1.53 mm. A 5 mm notch was made on an edge of the sample using a sharp razor blade. Tests were performed at a stretch rate of 0.05 s^{-1}. The critical stretch, λ_c, at the onset of crack propagation was recorded and used to calculate the strain energy density $w(\lambda_c)$ by integrating the stress–stretch curves of unnotched samples up to λ_c. The fracture energy, Γ_c, is equal to the energy release rate when the critical stretch is reached, *i.e.*, $\lambda = \lambda_c$, using the following equation:

$$\Gamma_c = w(\lambda_c) \times h_0$$

where h_0 is the original height of the sample between grips, usually around 5 mm.

Tensile tests

Tensile tests were performed on an Instron 5543 fitted with a 100 N load cell and pneumatic grips. Dogbone samples were cut out using a specimen die (ASTM D638 Type V). The gauge length of the central part was about 20 mm and the thickness of samples varied from 0.73 to 1.53 mm. Tests were performed at a strain rate of 0.05 s^{-1}. The strain rate is defined as $(dL/L_0)/dt$. Each set of samples was tested three times.

Real-time fluorescence tracking

To capture the bond scission of mechanophores during stretching, a camera (Mokose C100) with 4K resolution was used along with two different magnification-adjustable microlenses (Edmund Industrial Optics (EIO) and Hayear model HY180XA). While being stretched, the specimen was irradiated with a UV lamp (wavelength = 365 nm, 100 W). The specimen sat between the lamp and the camera. Two crossed polarizers were placed between the sample and the lamp and in front of the camera, respectively, to filter the background irradiation. Videos were recorded at manual mode with exposure parameters set to 1/30 s, ISO 100. After recording, the uncompressed raw video files were exported as images at one-second intervals. Blue channels of the images were analyzed using ImageJ. The intensity was measured by drawing a rectangle in the center of the specimen and the average values were used.

Characterization

Fluorescence spectroscopy was performed on an Agilent Cary Eclipse fluorescence spectrometer with a solid-state sample mounter. The excitation wavelength was set at 365 nm and the scanned emission wavelength ranged from 380 to 500 nm. The excitation and emission slits were both set as 2.5 nm.

Fluorescence imaging was done on an Olympus BX63 Microscope equipped with a fluorescence filter cube (U-FUNA) and observed using the DAPI observation method, with a magnification of 5× and a manual exposure time of 10 ms. The fluorescence intensity profile was plotted using ImageJ from the blue channel.

Glass transition temperatures were determined on a TA Instruments DSC250 under nitrogen (Fig. S1). Each sample (~5 mg) was equilibrated at 60 °C, cooled to −60 °C and then heated to 60 °C at a rate of 10 °C min^{-1}. The T_g was determined by the half-height method.

Results and discussion

Preparation of multiple network elastomers

MN elastomers were prepared in a similar manner as previously described[5] and detailed in the Experimental section. SN elastomers were synthesized by photopolymerization of EA in the presence of 1 mol% crosslinker and 0.004 mol% Irgacure 819 in chloroform (33 vol%). DN elastomers were subsequently prepared by swelling the said SN elastomers to equilibrium in a bath of EA monomer, BD crosslinker (0.01 mol%), and Irgacure 819 (0.004 mol%), followed by photopolymerization to form the second network (Fig. 1). This process of swelling and photopolymerization was carried out again for the DN elastomers to form a third network, yielding TN elastomers. When BD was used as the crosslinker for SN elastomers, the corresponding materials are termed SN-BD, DN-BD, and TN-BD; and when AM diacrylate was used as the crosslinker, the corresponding networks are termed SN-AM, DN-AM, and TN-AM. The most important factor governing the properties of a multiple network elastomer is the prestretch ratio λ_0, which is defined by the volume fraction of the first network in the multiple network ($\lambda_0 = (V_{MN}/V_{FN})^{1/3} = 1/{\Phi_{FN}}^{1/3}$). More steps of swelling and polymerization led to higher degrees of prestretch on the first network (Table 1). The effect of the type of the first network crosslinker on the prestretch ratio was negligible, with λ_0 being ~1.7 for DN and 2.6–2.7 for TN.

Toughness of multiple network elastomers

The mechanical properties of the SN, DN, and TN elastomers, including stiffness and toughness, were systematically evaluated to understand the role of the prestretch and crosslinker strength (Fig. 2). Stress–stretch curves for notched samples in pure shear geometry revealed clear differences in the mechanical performance with different degrees of prestretch (from SN,

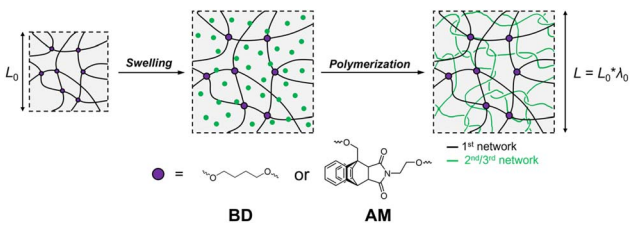

Fig. 1 Schematic illustration of the synthesis of multiple network elastomers *via* sequence(s) of swelling and polymerization. Black lines, green dots, and green lines represent the first network, ethyl acrylate monomer, and matrix network, respectively. The purple dots represent the butanediol diacrylate or anthracene–maleimide diacrylate crosslinkers.

Table 1 List of elastomer samples and their properties: prestretch ratio, λ_0; Young's modulus, E; fracture energy, Γ_c; and glass transition temperature, T_g

Sample	λ_0	E (MPa)	Γ_c (J m^{-2})	T_g (°C)
SN-BD	1	0.52 ± 0.09	0.27 ± 0.04	−13.1
DN-BD	1.74	0.89 ± 0.02	1.01 ± 0.13	−14.4
TN-BD	2.69	1.71 ± 0.05	2.89 ± 0.08	−14.6
SN-AM	1	0.62 ± 0.18	0.96 ± 0.17	−9.2
DN-AM	1.73	0.88 ± 0.01	1.65 ± 0.18	−13.3
TN-AM	2.64	1.79 ± 0.04	5.43 ± 0.74	−13.4

DN, to TN) and crosslinkers (AM and BD) in the first network (Fig. 2A). Quantitatively, the modulus increased from 0.5–0.6 MPa for SN to ~0.9 MPa for DN, and to 1.7–1.8 MPa in TN, showing that the prestretched first network effectively increased the stiffness of the overall network (Fig. 2B). The type of crosslinker, AM or BD, had a negligible effect on the modulus (Table 1), indicating similar network structures.

Crosslink density analyses provide additional insights into the network properties. For the SN-BD and SN-AM elastomers, swelling in toluene gave polymer volume fraction $\varphi \approx 0.15$, yielding crosslink density $\nu \approx 54$ mol m^{-3} from the Flory–Rehner equation, in good agreement with modulus-based estimates from the affine model (35 and 42 mol m^{-3}, respectively) and the phantom model (70 and 84 mol m^{-3}, respectively). The crosslink density of the single networks is stoichiometrically determined from the molar ratio of the diacrylate crosslinker to ethyl acrylate, giving a theoretical value of $\nu \approx 120$ mol m^{-3}. Detailed calculations are provided in the SI. The discrepancy between the experimental values and the theoretical one is attributed to network defects such as loops, which can account for more than 60% of strands even in model networks.[35] For DN and TN systems, ν is complicated by the prestretched, swollen nature of the first network that is interpenetrated by the subsequent entangled networks. Nonetheless, the modulus increases and swelling ratio decreases systematically from SN to DN to TN, consistent with increased effective crosslink density. Nonetheless, swelling ratios decrease from $Q \approx 6.7$ (SN) to 4.5 (DN) and 2.7 (TN), consistent with the observed increased stiffness as a result of increased effective crosslink density. ATR-FTIR spectra show disappearance of C–H (3100–3000 cm^{-1}) and C=C (1640–1680 cm^{-1}) absorptions (Fig. S2), indicating complete polymerization of acrylate double bonds. While FTIR confirms full monomer conversion, swelling and mechanical analyses provide more direct and quantitative evidence for crosslink density and multiple-network formation.

Increasing the extent of prestretch, λ_0, significantly improved the fracture energy, Γ_c (Fig. 2C). TN-BD exhibited the highest fracture energy, followed by DN-BD and SN-BD, indicating that the networks are effectively toughened through sacrificial bond scission in the prestretched first network.[5,8] Besides the multiple network strategy, toughening of an SN was also achieved by replacing the BD strong crosslinks with the AM weak crosslinks (Fig. 2C), suggesting an alternative toughening mechanism from mechanophore-enabled stress delocalization *via* selective decrosslinking.[31] Moreover, DN and TN were also effectively toughened by the implementation of AM mechanophores as weak crosslinks, as evidenced by the higher fracture energy values for AM-crosslinked networks compared to their respective controls. Notably, the fracture energy increased 20-fold—from 0.27 kJ m^{-2} for SN-BD to 5.4 kJ m^{-2} for TN-AM—indicating a synergistic toughening effect from the MN architecture coupled with weak crosslinks, which significantly improves stress redistribution capabilities that act to resist fracture. These findings highlight the role of weak, scissile AM crosslinks and increased prestretch in enhancing toughness through sacrificial and selective bond scission.

To gain mechanistic insights into the toughening mechanism, the extent of bond scission near the fracture surfaces was visualized and mapped *via* mechanofluorescence. The force-induced retro-Diels–Alder reaction of the AM mechanophore releases a fluorescent anthracene moiety (Fig. 3A). Fluorescence microscope images of SN-AM, DN-AM, and TN-AM samples revealed distinct gradient patterns of blue emission due to bond scission near the fracture surfaces (Fig. 3B). The breadth and amount of bond scission varied significantly among the networks, with TN-AM showing the widest and brightest

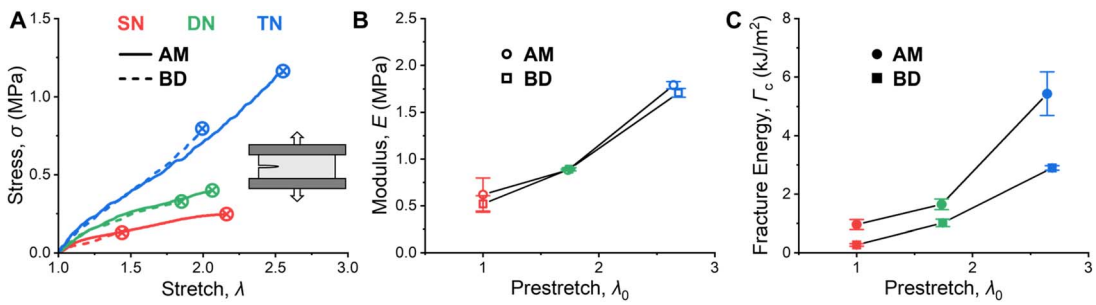

Fig. 2 Mechanical properties of the MN elastomers. (A) Representative stress–stretch curves of notched samples of MN elastomers in pure shear geometry (illustrated in the inset) with different degrees of prestretch, λ_0, and first network crosslinker. Red, green, and blue lines correspond to SN, DN, and TN, respectively. Solid and dashed lines correspond to AM and BD as the crosslinkers, respectively. (B) Young's modulus, E, from tensile tests for SN (red), DN (green), and TN (blue) over prestretch ratio, λ_0. (C) Fracture energy, Γ_c, obtained from pure shear fracture tests for SN (red), DN (green), and TN (blue) over prestretch ratio, λ_0. Solid circles and squares denote AM and BD as the crosslinkers, respectively. Error bars show the standard deviation with triplicates per experiment. Hollow circles and squares denote AM and BD as the crosslinkers, respectively.

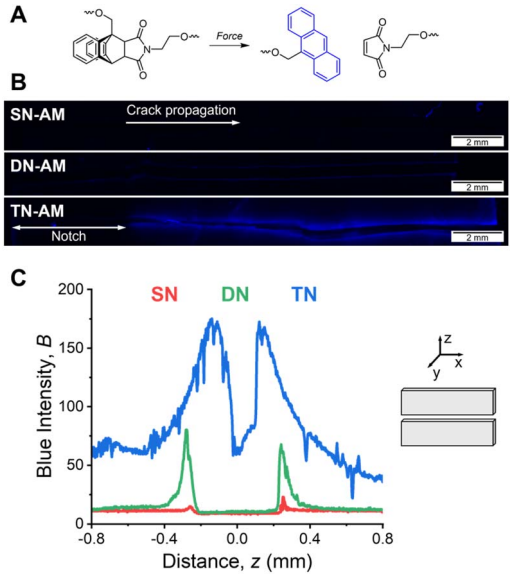

Fig. 3 Mapping the extent of bond scission in post-fracture MN elastomers *via* mechanofluorescence. (A) Force-induced retro-Diels–Alder reaction of AM mechanophore to release a fluorescent anthracene moiety. (B) Fluorescence microscope images of SN-AM, DN-AM, and TN-AM along the fracture surfaces. The crack propagated through the positive *x* direction. The notch length was about 4.7–5.0 mm. (C) Blue fluorescence intensity profiles in the center of two fracture surfaces of SN (red), DN (green), and TN (blue) in the *z* direction.

fluorescence. Quantification of fluorescence intensity perpendicular to the crack propagation direction (Fig. 3C) confirmed these observations. In SN-AM, only a narrow region (~30 μm) near the crack edge exhibited a low amount of fluorescence, indicating localized and limited bond scission. In contrast, DN-AM and TN-AM samples showed significantly broader bond scission zones with stronger fluorescence, with thickness approximating 100 μm and 400 μm, respectively. It is noteworthy that the AM concentration in TN-AM (6 mol m^{-3}) was much lower than that in SN-AM (121 mol m^{-3}) and DN-AM (23 mol m^{-3}), due to the dilution from the second and third networks. Therefore, the actual differences in the extent of mechanophore scission for SN-AM, DN-AM and TN-AM were much more distinct than what is shown in Fig. 3C. This trend where increasing the amount of prestretch increases both the intensity and spatial extent of fluorescence correlates with the fracture energy results, as TN-AM, with its greater fracture resistance, underwent more extensive bond scission, compared to SN-AM. It demonstrates that a higher degree of prestretch on the first network increases both the local concentration of strands amenable to scission and the volume of the network in which sacrificial bond scission occurs, synergistically contributing to the toughness enhancement.

Mechanic insights *via* mechanofluorescence

The stress–stretch curves for AM-containing SN, DN, and TN elastomers with different prestretch ratios exhibited similar tensile behavior at low stretch and slightly higher strengths compared to the control counterparts (Fig. 4A). The prestretched first network effectively increases the stiffness of the overall network, thus increasing the tensile stress at the same stretch. Since the first network is prestretched and thus stiffened by the diluting matrix network, it is safe to assume that the first network carries the majority of the stress.[8,36] To more accurately assess the mechanical response of the MNs, stress–stretch curves were normalized to account for the varying extent of prestretch, λ_0, on the first network. The tensile stress was normalized by the areal density of the first network strands, which are diluted by a factor of λ_0^2 by the matrix network, in the plane normal to the stretching direction. The stretch ratio was scaled by a factor of λ_0, corresponding to the actual stretch, $\lambda \cdot \lambda_0$, experienced by the first network in the stretching direction. Unified master curves were obtained, showing similar mechanical responses up to the point of fracture across all networks (Fig. 4B). This again demonstrates that increasing the degree of prestretch effectively improves the load-bearing capacity of the first network and its susceptibility to chain scission.

To gain deeper insights into the toughening mechanism, the stress-induced bond scission of mechanofluorescent AM was tracked in real time during uniaxial tensile extension. Plotting the blue fluorescence intensity as a function of macroscopic stretch revealed that the bond scission showed a stronger dependence on stretch ratio with greater prestretch (Fig. 4C). Similar to the mechanical response, the fluorescence profiles were also normalized to reflect the first network being the load-bearing component (Fig. 4D). The blue intensity was normalized by a factor of $\lambda^{0.5} \cdot \lambda_0^2$: the first term accounts for the area expansion of the observed side during stretching, and the second term accounts for the concentration of the AM mechanophore in the observed plane that is diluted by the matrix network. Clearly, DN-AM and TN-AM exhibited similar fluorescence build-up, with TN-AM ending up with stronger fluorescence. A unified threshold stretch ratio, that is, $\lambda \cdot \lambda_0 = 4$, for mechanophore activation was revealed, independent of the number of networks, indicating that mechanophore scission in the first network is governed by the actual stretch seen by the first network strands rather than the stretch ratio of the overall network. This is consistent with the unified mechanical response across different networks (Fig. 4B). Since the strain at break of SN-AM was smaller than the threshold strain for mechanochemical activation of AM, it did not exhibit significant fluorescence build-up upon elongation.

Spectral analysis of the fluorescence emission of the ruptured samples in the gauge section confirmed the AM scission *via* force-induced retro-Diels–Alder reaction, showing characteristic peaks of anthracene for DN-AM and TN-AM. SN-AM did not show any fluorescence signal, consistent with the real-time fluorescence measurements. The fluorescence intensity for TN-AM appears to be lower than that for DN-AM (Fig. 4E). As the AM content in TN-AM was 3.8 times lower than that in DN-AM due to higher λ_0, the actual amount of AM scission in TN-AM was higher than that in DN-AM (Fig. 4F). TN-AM achieved 37% AM activation, while DN-AM reached 13%. This further confirms that greater prestretch increases the fraction of strands under sufficient tension to undergo mechanochemical reactions.

The fraction of activated mechanophores and the work of fracture, $W_f \cdot \lambda_0^3$ are plotted against the prestretch ratio, λ_0

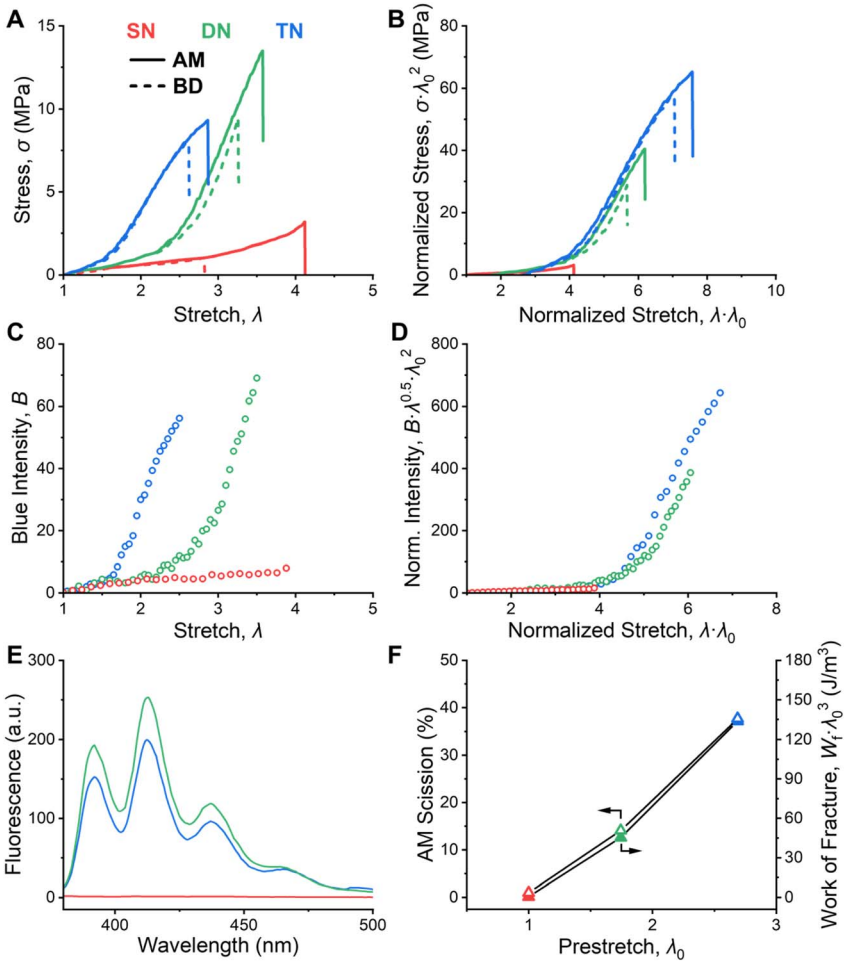

Fig. 4 Real-time visualization of AM mechanophore scission in tensile testing. (A) Representative stress–stretch curves of dog bone samples of MN elastomers with different degrees of prestretch λ_0 and first network crosslinker. Red, green, and blue lines correspond to SN, DN, and TN, respectively. Solid and dashed lines correspond to AM and BD as the crosslinkers, respectively. (B) Normalized stress–stretch curves by accounting for the prestretch ratio, λ_0, of the first network. (C) Fluorescence blue intensity profiles of the SN-AM (red), DN-AM (green), and TN-AM (blue) elastomers as a function of stretch ratio. (D) Normalized fluorescence blue intensity profiles as a function of normalized stretch ratio. (E) Fluorescence spectra for the ruptured samples in the gauge section. (F) The fraction of mechanically activated AM mechanophore in the ruptured samples near the gauge section and the work of fracture normalized by the volume fraction of the first network, $W_f \cdot \lambda_0^3$, as a function of pre-stretch ratio.

(Fig. 4F). Here the work of fracture has been normalized by the volume fraction of the first network, $\Phi_{FN} = 1/\lambda_0^3$, to represent the work done to the load-bearing network. The quantitative correlation here underscores that bond scission in the first network is a major contributor to the overall toughness of the MN elastomers. In all, while TN-AM exhibited lower elongation at break compared to DN-AM, the actual stretch experienced by the first network strands in TN-AM was higher, which increased the fraction of mechanically labile strands in the first network. This increases the extent of stress redistribution and thus resistance to rupture.

Synergistic interplay between mechanophores and multiple network structure

The effects of crosslinker strength and network topology govern the fracture behavior and toughening mechanism of elastomers. As illustrated in the schematic (Fig. 5), elastomers with strong crosslinks fracture through random bond scission. In a conventional SN with strong crosslinks, fracture occurs along a narrow zone where stress is localized and strands near the crack tip break catastrophically (Fig. 5A). By contrast, replacing strong crosslinks with weak, force-responsive ones, *i.e.*, AM mechanophores, changes the failure dynamics. In an SN with weak AM crosslinks, bond scission still occurs near the crack tip but is biased toward the mechanically weaker AM crosslinks (Fig. 5B). This decrosslinking mechanism mitigates the local stress through strand lengthening,[31] which ultimately increases the fracture energy as it scales with square root of strand length.[2,3]

When a stretchable, interpenetrating network is introduced to form an MN elastomer, the highly crosslinked first network becomes prestretched and sacrificial, breaking over a much broader zone during fracture (Fig. 5C). This delocalization of

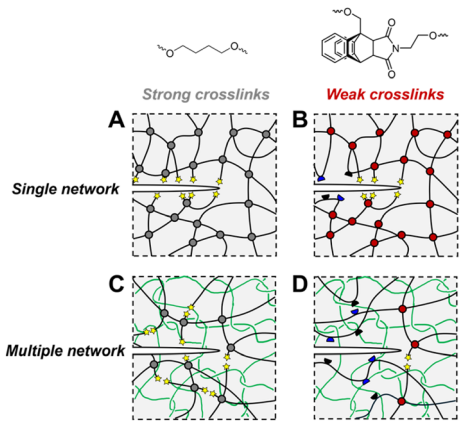

Fig. 5 Schematic illustration for different scenarios upon network fracture. (A) In a single network, a series of chain scission occurs as the crack propagates. (B) In a single network with weak AM crosslinks, bond scission occurs near the crack tip but is preferred over other covalent bonds, leading to strand lengthening that delocalizes stress. (C) In a conventional multiple network, the stress is redistributed through bond scission over a large area, delaying the onset of fracture. (D) In a mechanophore-crosslinked multiple network, localized stress is further alleviated *via* stress-induced mechanophore crosslinker dissociation that lengthens the strands across a broad region.

stress *via* bond scission delays the onset of crack propagation and improves toughness—yet this process remains random. When the AM mechanophores as weak crosslinks are embedded within an MN framework, the strands extend in length as the crosslinks dissociate under stress (Fig. 5D), resulting in a further increase in toughness.

Thus, the synergy between multiple networks and mechanophores enables a dual-mode toughening strategy. The MN structure enables delocalized, sacrificial scission in the first network, while the incorporation of mechanophores as weak crosslinks alleviates and distributes stress through stress-induced strand extension. Together, they enable simultaneous mechanical reinforcement and real-time, visualizable quantification of damage, offering a powerful platform for the design of self-reporting, resilient soft materials.

Conclusions

We have prepared tough, stress-reporting elastomers by integrating mechanophore crosslinkers within an MN architecture and elucidated the toughening mechanism. Mechanophore-containing MN elastomers exhibited significantly enhanced toughness compared to the conventional single network, owing to sacrificial and selective bond scission in the prestretched first network. The AM mechanophores enabled real-time visualization of stress-induced bond breakage *via* mechanofluorescence, providing direct mechanistic insights into the fracture process. Mechanical and optical analyses revealed that the first network serves as the primary load-bearing component and is selectively fractured under loading, contributing to stress delocalization. Fluorescence imaging showed that the extent and intensity of mechanophore scission increased with the degree of prestretch, correlating well with the toughness in both notched and unnotched samples. Notably, TN elastomers with the highest prestretch achieved 37% mechanophore activation post-fracture, demonstrating the amplification effect of the MN structure on mechanochemical responsiveness.

This study provides fundamental understanding of how crosslink strength and network hierarchy govern stress distribution and fracture resistance in soft materials, showing that prestretch and weak crosslinks cooperatively enhance stress redistribution and strand lengthening. It establishes a powerful framework for designing multifunctional elastomers that combine mechanical resilience with damage reporting capabilities. The integration of weak, force-responsive crosslinks with MN topology offers a dual-mode toughening platform that integrates mechanical reinforcement with quantitative stress mapping—a paradigm shift for designing smart elastomers.

Looking forward, this strategy opens up exciting opportunities to design next-generation elastomers with tailored mechanical and optical properties. Future efforts may explore a broader range of mechanophore chemistries, reversible or self-healing network architecture, and deep dive into fracture mechanics of elastomers. The approach described here lays the groundwork for smart, self-sensing, and damage-tolerant materials suitable for use in structural health monitoring, soft robotics, and protective coatings, where real-time stress feedback and mechanical robustness are both essential.

Author contributions

Z. W. and J. W. conceived the project. Z. W., Y. W., and M.-C. W. conducted the material synthesis and characterization. Z. W., Y. W., and Z. F. conducted the tensile and fracture tests. Z. W. and Y. W. performed the fluorescence spectroscopic and microscopic analyses. Y. W. and M.-C. W. measured the glass transitions. Z. W. wrote the original draft, while all authors contributed to the review and editing of the manuscript.

Conflicts of interest

There are no conflicts to declare.

Data availability

The data supporting this article, including experimental details, DSC curves, IR spectra, stress–stretch curves, and fluorescence spectra, have been included as part of the SI.

Supplementary information is available. See DOI: **https://doi.org/10.1039/d5ta04890g**.

Acknowledgements

This work was supported by the National Science Foundation under grant no. CHE-2204079. Z. F. acknowledges the National Science Foundation for funding support (DMR-2210184). J. W. acknowledges the Alfred P. Sloan Foundation for a Sloan Research Fellowship (FG-2023-20341) and the Camille and

Henry Dreyfus Foundation for a Camille Dreyfus Teacher-Scholar Award (TC-24-087).

References

1 P. J. Flory, *Principles of Polymer Chemistry*, Cornell university press, 1953.
2 G. J. Lake and A. G. Thomas, *Proc. Roy. Soc. Lond. Math. Phys. Sci.*, 1967, **300**, 108–119.
3 A. K. Bhowmick, *Polym. Rev.*, 1988, **28**, 339–370.
4 J. Kim, G. Zhang, M. Shi and Z. Suo, *Science*, 2021, **216**, 212–216.
5 E. Ducrot, Y. Chen, M. Bulters, R. P. Sijbesma and C. Creton, *Science*, 2014, **344**, 186–189.
6 J. P. Gong, Y. Katsuyama, T. Kurokawa and Y. Osada, *Adv. Mater.*, 2003, **15**, 1155–1158.
7 S. Nakagawa, D. Aoki, Y. Asano and N. Yoshie, *Adv. Mater.*, 2023, **35**, 2301124.
8 J. Slootman, C. J. Yeh, P. Millereau, J. Comtet and C. Creton, *Proc. Natl. Acad. Sci. U. S. A*, 2022, **119**, 1–11.
9 Y. Chen, G. Sanoja and C. Creton, *Chem. Sci.*, 2021, **12**, 11098–11108.
10 Y. Chen, G. Mellot, D. Van Luijk, C. Creton and R. P. Sijbesma, *Chem. Soc. Rev.*, 2021, **50**, 4100–4140.
11 G. De Bo, *Macromolecules*, 2020, **53**, 7615–7617.
12 E. Izak-Nau, D. Campagna, C. Baumann and R. Göstl, *Polym. Chem.*, 2020, **11**, 2274–2299.
13 J. Li, C. Nagamani and J. S. Moore, *Acc. Chem. Res.*, 2015, **48**, 2181–2190.
14 N. Willis-Fox, E. Rognin, T. A. Aljohani and R. Daly, *Chem*, 2018, **4**, 2499–2537.
15 M. A. Ghanem, A. Basu, R. Behrou, N. Boechler, A. J. Boydston, S. L. Craig, Y. Lin, B. E. Lynde, A. Nelson, H. Shen and D. W. Storti, *Nat. Rev. Mater.*, 2021, **6**, 84–98.
16 N. Deneke, M. L. Rencheck and C. S. Davis, *Soft Matter*, 2020, **16**, 6230–6252.
17 C. E. Diesendruck and J. S. Moore, in *Self-Healing Polymers: From Principles to Applications*, Wiley-VCH, 2013, DOI: DOI: 10.1002/9783527670185, ch. 8, pp. 193–214.
18 T. Wang, H. Wang, L. Shen and N. Zhang, *Polym. Chem.*, 2021, **12**, 3832–3841.
19 A. R. Sulkanen, J. Sung, M. J. Robb, J. S. Moore, N. R. Sottos and G. Y. Liu, *J. Am. Chem. Soc.*, 2019, **141**, 4080–4085.
20 Z. Chen, F. Ye, T. Shao, Y. Wu, M. Chen, Y. Zhang, X. Zhao, B. Zou and Y. Ma, *Macromolecules*, 2022, **55**, 2310–2319.
21 H. Qian, N. S. Purwanto, D. G. Ivanoff, A. J. Halmes, N. R. Sottos and J. S. Moore, *Chem*, 2021, **7**, 1080–1091.
22 Y. Vidavsky, S. J. Yang, B. A. Abel, I. Agami, C. E. Diesendruck, G. W. Coates and M. N. Silberstein, *J. Am. Chem. Soc.*, 2019, **141**, 10060–10067.
23 Y. Chen, C. Joshua Yeh, Y. Qi, R. Long and C. Creton, *Sci. Adv.*, 2020, **6**, 1–9.
24 Y. Sun, W. J. Neary, Z. P. Burke, H. Qian, L. Zhu and J. S. Moore, *J. Am. Chem. Soc.*, 2022, **144**, 1125–1129.
25 G. I. Peterson, J. Lee and T.-L. Choi, *Macromolecules*, 2019, **52**, 9561–9568.
26 T.-G. Hsu, J. Zhou, H. W. Su, B. R. Schrage, C. J. Ziegler and J. Wang, *J. Am. Chem. Soc.*, 2020, **142**, 2100–2104.
27 Y. Lin, T. B. Kouznetsova and S. L. Craig, *J. Am. Chem. Soc.*, 2020, **142**, 2105–2109.
28 S. Wang, H. K. Beech, B. H. Bowser, T. B. Kouznetsova, B. D. Olsen, M. Rubinstein and S. L. Craig, *J. Am. Chem. Soc.*, 2021, **143**, 3714–3718.
29 Z. Wang, X. Zheng, T. Ouchi, T. B. Kouznetsova, H. K. Beech, S. Av-Ron, T. Matsuda, B. H. Bowser, S. Wang and J. A. Johnson, *Science*, 2021, **374**, 193–196.
30 H. Sakai, D. Aoki, K. Seshimo, K. Mayumi, S. Nishitsuji, T. Kurose, H. Ito and H. Otsuka, *ACS Macro Lett.*, 2020, **9**, 1108–1113.
31 S. Wang, Y. Hu, T. B. Kouznetsova, L. Sapir, D. Chen, A. Herzog-Arbeitman, J. A. Johnson, M. Rubinstein and S. L. Craig, *Science*, 2023, **380**, 1248–1252.
32 J. A. Syrett, G. Mantovani, W. R. S. Barton, D. Price and D. M. Haddleton, *Polym. Chem.*, 2010, **1**, 102–106.
33 A. C. Overholts, M. E. McFadden and M. J. Robb, *Macromolecules*, 2022, **55**, 276–283.
34 C. P. Kabb, C. S. O'Bryan, C. D. Morley, T. E. Angelini and B. S. Sumerlin, *Chem. Sci.*, 2019, **10**, 7702–7708.
35 M. Zhong, R. Wang, K. Kawamoto, B. D. Olsen and J. A. Johnson, *Science*, 2016, **353**, 1264–1268.
36 P. Millereau, E. Ducrot, J. M. Clough, M. E. Wiseman, H. R. Brown, R. P. Sijbesma and C. Creton, *Proc. Natl. Acad. Sci. U. S. A*, 2018, **115**, 9110–9115.

